

AD A045545

RADC-TR-77-165
Interim Report
May 1977



PHOTON LIMITATIONS IN IMAGING AND IMAGE RESTORATION

Stanford University

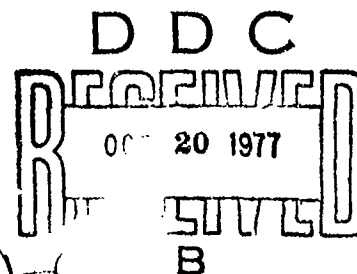
Approved for public release; distribution unlimited.

Sponsored by
Defense Advanced Research Projects Agency (DoD)
ARPA Order No. 2646

The views and conclusions contained in this document are those of the authors and should not be interpreted as necessarily representing the official policies, either expressed or implied, of the Defense Advanced Research Projects Agency or the U. S. Government.

AD No. _____
DDC FILE COPY

ROME AIR DEVELOPMENT CENTER
Air Force Systems Command
Griffiss Air Force Base, NY York 13441



This report has been reviewed by the RADC Information Office (OI) and is releasable to the National Technical Information Service (NTIS). At NTIS it will be releasable to the general public including foreign nations.

This report has been reviewed and is approved for publication.

APPROVED:



EDWARD C. MAHEN Jr., Captain, USAF
Act Engineer

Do not return this copy. Retain or destroy.

PHOTON LIMITATIONS IN IMAGING AND IMAGE RESTORATION

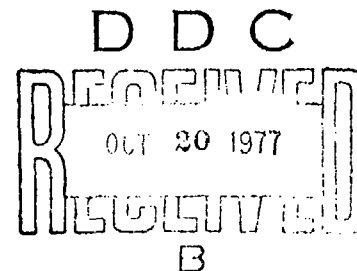
J. W. Goodman
J. F. Belsher

Contractor: Stanford University
Contract Number: F30602-75-C-0228
Effective Date of Contract: 23 March 1976
Contract Expiration Date: 28 February 1978
Short Title of Work: Photon Limited Image
Restoration
Program Code Number: 7E20
Period of Work Covered: Jul 76 - Jan 77

Principal Investigator: J. W. Goodman
Phone: 415 497-3304
Project Engineer: Capt E. Mahen
Phone: 315 330-3145

Approved for public release;
distribution unlimited.

This research was supported by the Defense Advanced Research Projects Agency of the Department of Defense and was monitored by Captain Edward C. Mahen (OCSE), Griffiss AFB NY 13441 under Contract F30602-75-C-0228.



UNCLASSIFIED

SECURITY CLASSIFICATION OF THIS PAGE (When Data Entered)

REPORT DOCUMENTATION PAGE		READ INSTRUCTIONS BEFORE COMPLETING FORM	
1. REPORT NUMBER	2. GOVT ACCESSION NO.	3. RECIPIENT'S CATALOG NUMBER	
18. RADC-TR-77-165			
4. TITLE (and Subtitle)	5. TYPE OF REPORT & PERIOD COVERED	9.	
6. PHOTON LIMITATIONS IN IMAGING AND IMAGE RESTORATION	Interim Report		
	1 Jul 76 - 1 Jan 77		
	6. PERFORMING ORG. REPORT NUMBER		
	N/A		
7. AUTHOR(s)	8. CONTRACT OR GRANT NUMBER(s)		
10. J. W. Goodman J. F. Belsher	15. F30602-75-C-0228		
9. PERFORMING ORGANIZATION NAME AND ADDRESS	10. PROGRAM ELEMENT, PROJECT, TASK AREA & WORK UNIT NUMBERS		
Stanford University Stanford CA 94305	62301E 26460405		
11. CONTROLLING OFFICE NAME AND ADDRESS	12. REPORT DATE		
Defense Advanced Research Projects Agency 1400 Wilson Blvd Arlington VA 22209	11. May 1977		
14. MONITORING AGENCY NAME & ADDRESS (if different from Controlling Office)	13. NUMBER OF PAGES		
Rome Air Development Center (OCSE) Griffiss AFB NY 13441	30		
16. DISTRIBUTION STATEMENT (of this Report)	18. SECURITY CLASS. (of this report)		
Approved for public release; distribution unlimited.	UNCLASSIFIED		
17. DISTRIBUTION STATEMENT (of the abstract entered in Block 20, if different from Report)	19. DECLASSIFICATION/DOWNGRADING SCHEDULE		
Same	N/A		
18. SUPPLEMENTARY NOTES			
RADC Project Engineer: Captain E. Mahen (OCSE)			
19. KEY WORDS (Continue on reverse side if necessary and identify by block number)			
Speckle Interferometry Amplitude Interferometry Image Processing			
20. ABSTRACT (Continue on reverse side if necessary and identify by block number)			
This report describes progress made in image quality factors, limiting performance of speckle and amplitude interferometry, and formulation of a least-squares filtering problem for space-variant degradations. This work is in photon-limited imaging systems, their limitations, and the restorability of their imagery.			

DD FORM 1 JAN 73 1473

EDITION OF 1 NOV 68 IS OBSOLETE

UNCLASSIFIED

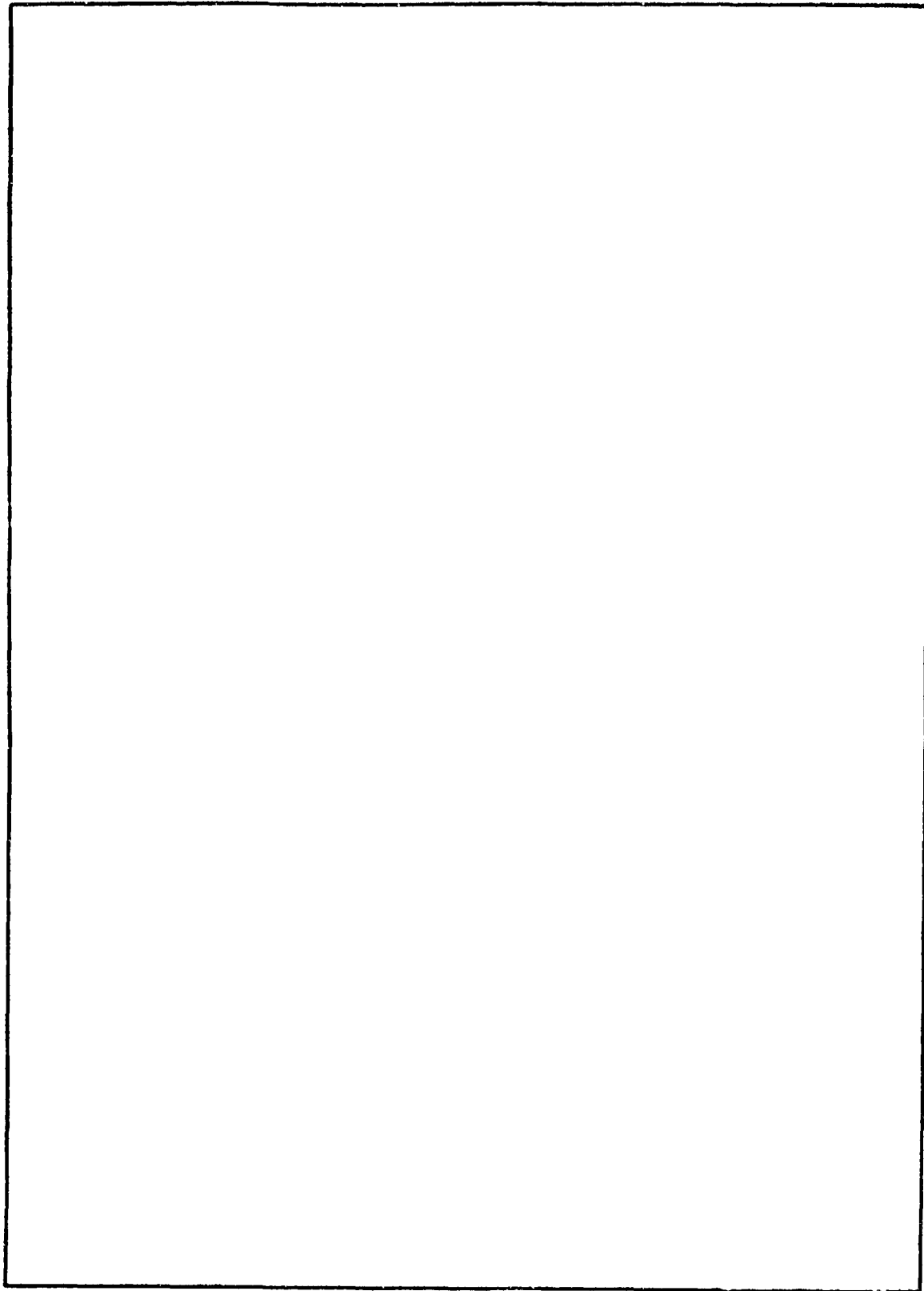
SECURITY CLASSIFICATION OF THIS PAGE (When Data Entered)

332 550

11/15

UNCLASSIFIED

SECURITY CLASSIFICATION OF THIS PAGE(When Data Entered)



UNCLASSIFIED

SECURITY CLASSIFICATION OF THIS PAGE(When Data Entered)

I. INTRODUCTION

In this report we describe progress made in three different areas of research. In all cases, our two previous technical reports [1,2] are recommended background, and we shall freely call upon results derived in them. First, a new image quality factor Q is defined, and a variety of curves of Q vs. the average number of image photoevents, \bar{N} , are given for both precompensated and postcompensated imagery. Second, a comparison of the photon noise-limited performance of amplitude interferometry and speckle interferometry is presented. Lastly, we describe the current status of our formulation of the least-squares filtering problem when the filter is allowed to be space-variant or nonlinear.

II. A NEW QUALITY FACTOR Q

In previous reports we have used a quality factor Q defined by

$$Q = \frac{(\bar{N})^2 \iint_{-\infty}^{\infty} |\hat{S}|^2 \hat{\Phi}_0 d\Omega_X d\Omega_Y}{\epsilon} - 1 \quad (1)$$

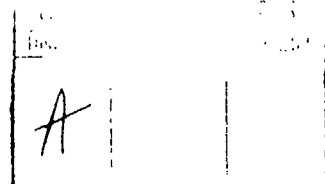
where

\bar{N} = the mean number of photoevents detected in the entire image;

\hat{S} = the transfer function[†] of the ideal system, which is taken to be that of a diffraction-limited telescope with a circular aperture;

Ω_X and Ω_Y = spatial frequencies measured in cycles per radian of arc in the sky;

[†] Here and throughout this report, quantities with a $\hat{}$ over them are normalized to have value unity at the origin.



\hat{B} = total blur OTF

$\hat{\phi}_0$ = the normalized average energy spectral density associated with the object ensemble; and

ϵ = the mean-squared error associated with the restored image.

The mean-squared error was stated explicitly as being [2]

$$\epsilon = \iint_{-\infty}^{\infty} \frac{(\bar{N})^2 |\hat{S}|^2 \hat{\phi}_0}{1 + \bar{N} |\hat{B}|^2 \hat{\phi}_0} d\Omega_X d\Omega_Y \quad (2)$$

Note that the numerator of the fraction in expression (1) is simply the ideal signal power. It is necessary to subtract unity from the ratio due to the fact that in the limit where $\bar{N} \rightarrow 0$, the denominator ϵ approaches the numerator, whereas we desire a quality measure that goes to zero as \bar{N} goes to zero.

Previous expressions for the transfer function of the restoration filter have been presented in normalized form [1, p.16]

$$\hat{H}(\Omega_X, \Omega_Y) = \frac{(1 + \bar{N}) \hat{S} \hat{B}^* \hat{\phi}_0}{1 + \bar{N} |\hat{B}|^2 \hat{\phi}_0} \quad (3)$$

In order to arrive at a more satisfying definition of the quality factor Q we have found it convenient to deal with un-normalized quantities in some cases. The form of the un-normalized optimum transfer function can be shown to be

$$H(\Omega_X, \Omega_Y) = \frac{k \bar{N} \hat{S} \hat{B}^* \hat{\phi}_0}{1 + \bar{N} |\hat{B}|^2 \hat{\phi}_0} \quad (4)$$

with k a constant given explicitly by

$$k = \frac{h \bar{\nu}}{\eta T b_0} \quad (5)$$

where

h = Planck's constant

$\bar{\nu}$ = the mean optical frequency

η = the quantum efficiency

T = the image integration time

b_0 = the volume under the blur spread function $b(x,y)$, i.e.,

$$b_0 = \iint_{-\infty}^{\infty} b(x,y) dx dy \quad (6)$$

When the constant k is included in the expression for the optimum transfer function H , the expression for the mean-squared error becomes

$$\epsilon = \iint_{-\infty}^{\infty} \frac{k^2 \bar{N} |\hat{S}|^2 \hat{\phi}_0}{1 + \bar{N} |\hat{B}|^2 \hat{\phi}_0} d\Omega_X d\Omega_Y \quad (7)$$

This expression for ϵ serves as a useful and meaningful representation of the "noise" associated with the restored image, where the term "noise" is used here in a general sense to include both random fluctuations introduced by the random positions and random numbers of the photoevents, and residual blur in the restored image.

The numerator or "signal" component of the new expression for Q is also modified to be more reasonable. Rather than using the "ideal" signal power in the image, we use instead the actual signal power in the restored image. Thus the numerator of the expression for Q becomes

$$\mathcal{S} = \bar{N}^2 \iint_{-\infty}^{\infty} |\hat{B}H|^2 \hat{\phi}_0 d\Omega_X d\Omega_Y \quad (8)$$

where H is the un-normalized restoration transfer function. The new quality factor Q thus becomes

$$Q = \frac{\delta}{\varepsilon} = \frac{(\bar{N})^2 \iint_{-\infty}^{\infty} |\hat{B}H|^2 \hat{\phi}_0 d\Omega_X d\Omega_Y}{(\bar{N})^2 k^2 \iint_{-\infty}^{\infty} \frac{|\hat{S}|^2 \hat{\phi}_0}{1 + \bar{N} |\hat{B}|^2 \hat{\phi}_0} d\Omega_X d\Omega_Y} \quad (9)$$

Substituting Eq.(4) for H , we obtain

$$Q = \frac{(\bar{N})^2 \iint_{-\infty}^{\infty} \frac{|\hat{B}|^4 |\hat{S}|^2 \hat{\phi}_0^3}{(1 + \bar{N} |\hat{B}|^2 \hat{\phi}_0)^2} d\Omega_X d\Omega_Y}{\iint_{-\infty}^{\infty} \frac{|\hat{S}|^2 \hat{\phi}_0}{1 + \bar{N} |\hat{B}|^2 \hat{\phi}_0} d\Omega_X d\Omega_Y} \quad (10)$$

The new quantity parameter defined above is more reasonable in its behavior than the parameter used previously. Its most desirable properties are that $Q \rightarrow 0$ as $\bar{N} \rightarrow 0$ and Q ultimately increases in proportion to \bar{N} as \bar{N} grows arbitrarily large. This latter property is expected for any measure of the mean-squared signal-to-noise ratio of a Poisson-related variable.

We now present some specific curves of the new Q vs. \bar{N} for several cases of specific interest. The cases treated here are precisely the same ones treated in our last technical report [2], and the reader may wish to consult that reference for a more detailed discussion of the assumptions behind each set of curves. In all cases it is assumed that the object of interest is an ideal point source ($\hat{\phi}_0 = 1$). Figure 1 shows plots of $\log_{10} Q$ vs. $\log_{10} \bar{N}$ for three different cases of post-compensation. In part (a) it is assumed that a long-time-averaged image is recorded. Various values of the atmospheric coherence diameter r_0 are shown, the case $r_0 = \infty$ corresponding to a perfect diffraction-

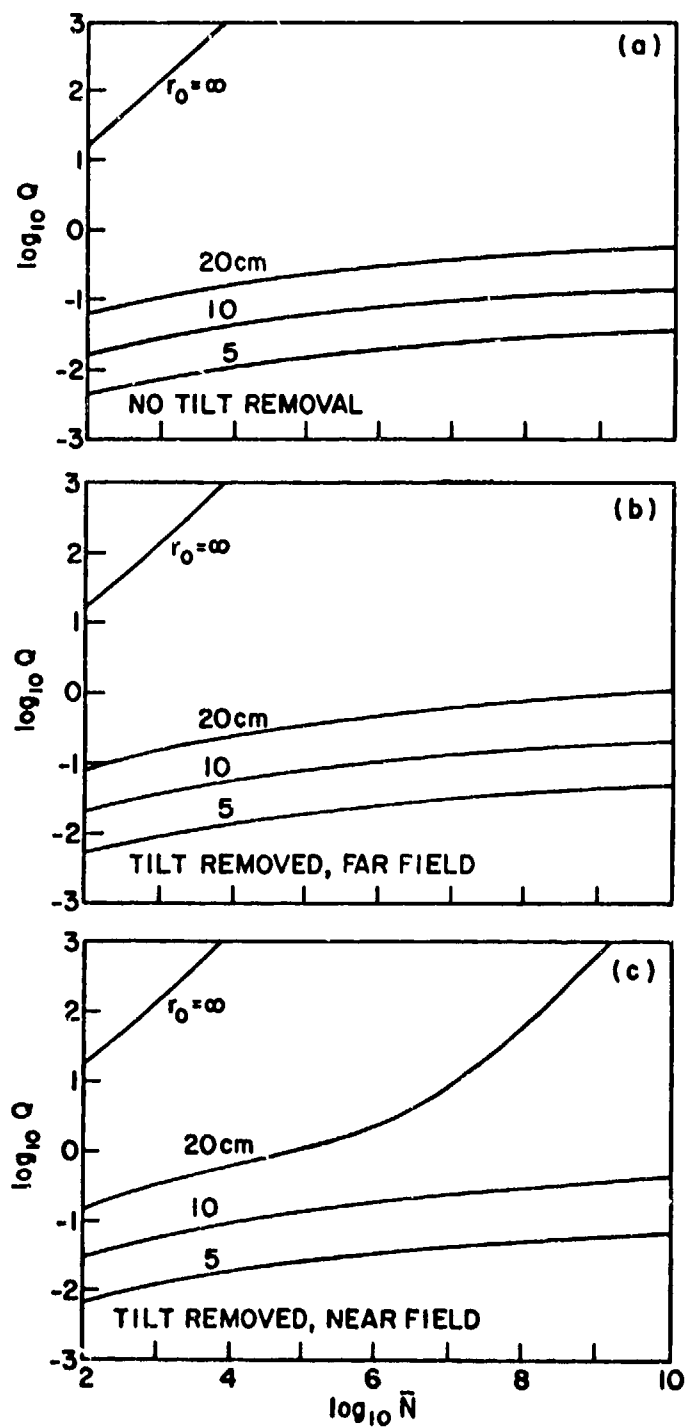


Fig. 1: Q vs. \bar{N} for three different cases of postcompensation: (a) no tilt removal; (b) tilt removal, far field; (c) tilt removal, near field.

limited image, with only photon noise limiting the restoration. In part (b), it is assumed that a perfect tilt-removing mirror is used as a pre-compensator, and that "far field" atmospheric propagation conditions hold. Finally, in part (c), tilt removal is again assumed, but "near field" propagation conditions hold. Note the break point in the $r_0 = 20$ cm curve, after which Q increases in proportion to \bar{N} . All curves have such a break point for large enough \bar{N} , but only for the $r_0 = 20$ cm curve does this point fall within the range of \bar{N} shown here.

For comparison purposes, we show in Figure 2 the corresponding curves of Q vs. \bar{N} when no post-compensation is applied. Comparison of Figs. 1 and 2 thus provides an indication of how much gain in quality factor is provided by postcompensation at each level of \bar{N} .

In presenting the results for precompensation alone and for combined pre- and postcompensation, the theoretical development presented in reference [2] has been followed. Specifically, a shearing interferometer with 317 subapertures has been assumed. The ratio of image integration time T to wavefront sensor integration time τ has been taken to be 10^4 , and errors introduced by the temporal dynamics of the atmosphere have not been included. The parameter β represents the fraction of photons sent to the wavefront sensor, while $1-\beta$ represents the fraction sent to the image detection plane.

The curves of Fig. 3 show $\log_{10} Q$ vs. $\log_{10} \bar{N}$ for several cases of precompensation alone (i.e., no postcompensation filtering used). Part (a) assumes that $\beta = 0.9$ and shows the dependence of Q on \bar{N} for several values of the atmospheric coherence diameter r_0 . Part (b) assumes that $r_0 = 10$ cm and shows the corresponding dependence for three

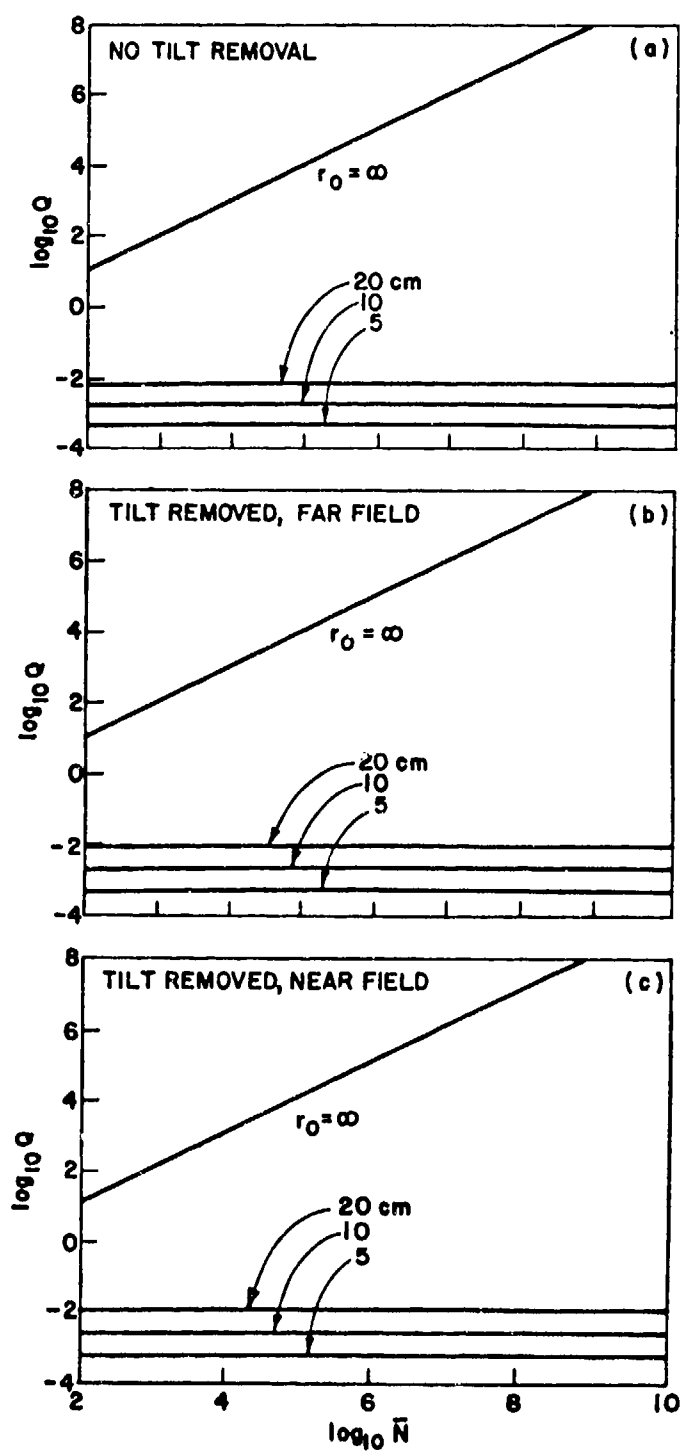


Fig. 2: Q vs. \bar{N} with no precompensation or postcompensation: (a) no tilt removal; (b) tilt removal, far field; (c) tilt removal, near field.

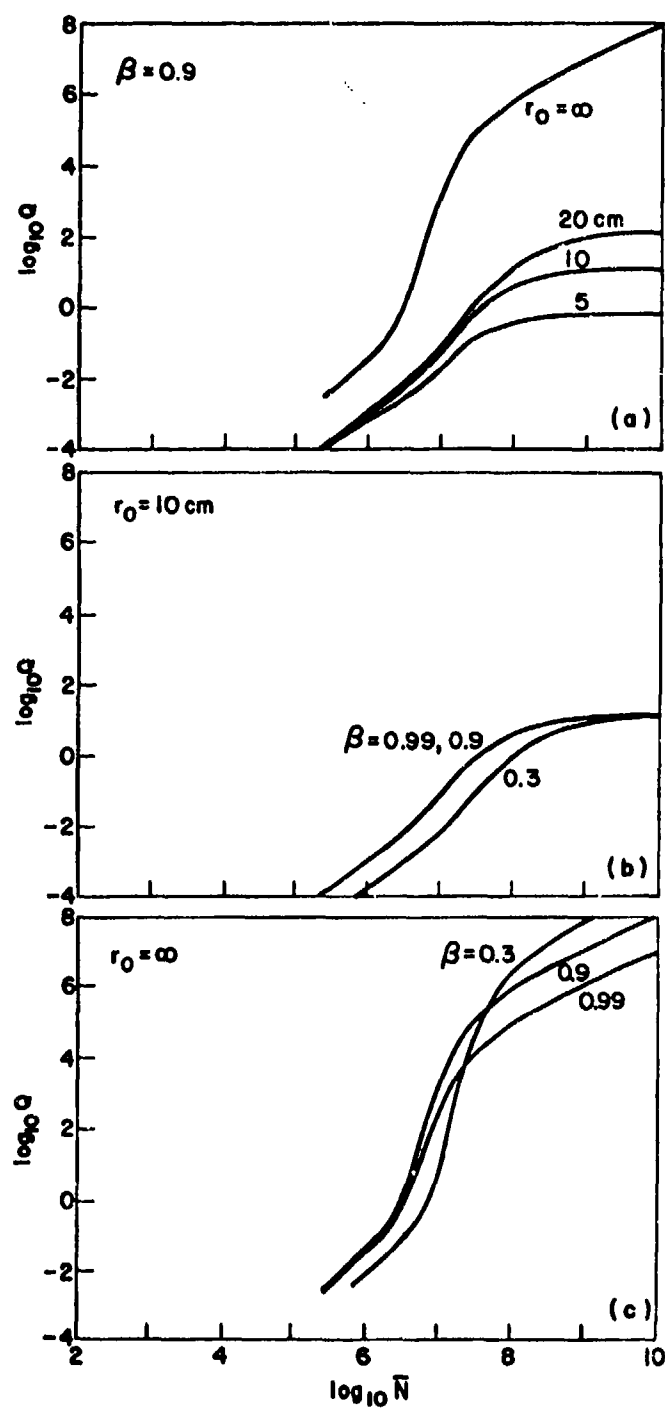


Fig. 3: Q vs. \bar{N} with precompensation alone:
 (a) $\beta=0.9$, several values of r_0 ;
 (b) $r_0=10$ cm, several values of β ;
 (c) $r_0=\infty$, several values of β .

values of β (0.3, 0.9, 0.99). Part (c) assumes that $r_0 = \infty$ (no atmosphere) and again shows the dependence of Q on \bar{N} for the same three values of β . Note in the curves of part (b), in the absence of any post-compensation the curves appear to saturate at a finite value of Q , a property attributable to the wavefront fitting errors, which do not depend on \bar{N} . Such errors are not present when $r_0 = \infty$, hence the curves of part (c) continue to increase with \bar{N} . Note also that for the curves of part (b), the large values of β (0.9 and 0.99) achieve the best values of Q for a given \bar{N} , but when no atmosphere is present (part (c)), better image quality is ultimately achieved (for large \bar{N}) if less light is diverted to the wavefront sensor. Since in the latter case the wavefront sensor serves no useful purpose, these results make good sense.

Figure 4 shows several results of interest for combined precompensation and postcompensation. In part (a) of the figure, r_0 is taken to be 10 cm, and the dependence of Q on \bar{N} is shown for several values of β . The curves do not saturate in this case at large \bar{N} , due to the fact that post-compensation removes the effects of wavefront fitting errors. In part (b) of the figure, $\log_{10} Q$ is plotted vs. the splitting ratio β for several fixed values of \bar{N} . At high light levels (large \bar{N}), an extremely broad maximum is found, so the exact value of β is not of great consequence. At low light levels (smaller \bar{N}), a narrower maximum develops in the region of large β (i.e., most of the light sent to the wavefront sensor). Finally, in part (c), we have $\log_{10} Q$ vs. $\log_{10} \bar{N}$ for a fixed splitting ratio ($\beta = 0.9$) and for several values of r_0 . The curves for $r_0 = \infty$ and $r_0 = 20$ cm are almost indistinguishable, while Q is

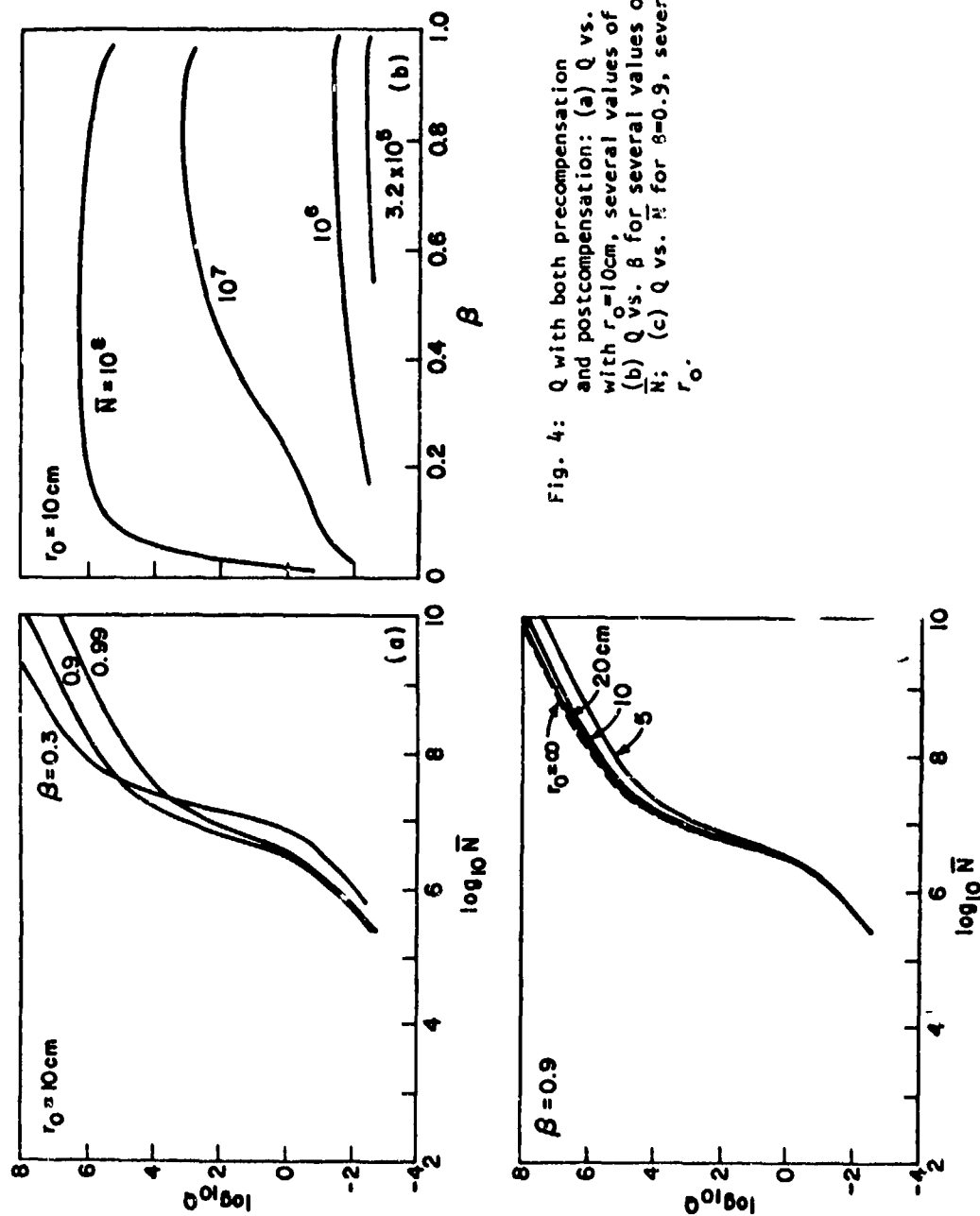


Fig. 4: Q with both precompensation and postcompensation: (a) Q vs. \bar{N} with $r_0 = 10\text{cm}$, several values of β ; (b) Q vs. \bar{N} for several values of β ; (c) Q vs. \bar{N} for $\beta = 0.9$, several r_0 .

noticeably reduced by smaller r_0 , a consequence of the increased fitting errors.

Lastly, in Figure 5 we plot several curves of $\log_{10} Q$ vs. $\log_{10} \bar{N}$ for comparison purposes. In all cases r_0 is taken to be 10 cm. Curve (a) corresponds to the case of both precompensation and postcompensation, with $\beta = 0.9$. Curve (b) corresponds to precompensation only, again with $\beta = 0.9$. Curve (c) corresponds to tilt removal and postcompensation ($\beta = 0$, near field propagation), while (d) applies for postcompensation only. Curve (e) shows the result for tilt removal only (no postcompensation), while curve (f) corresponds to no compensation whatsoever. Examination of these curves reveals the gain in quality factor achieved by each type of image compensation.

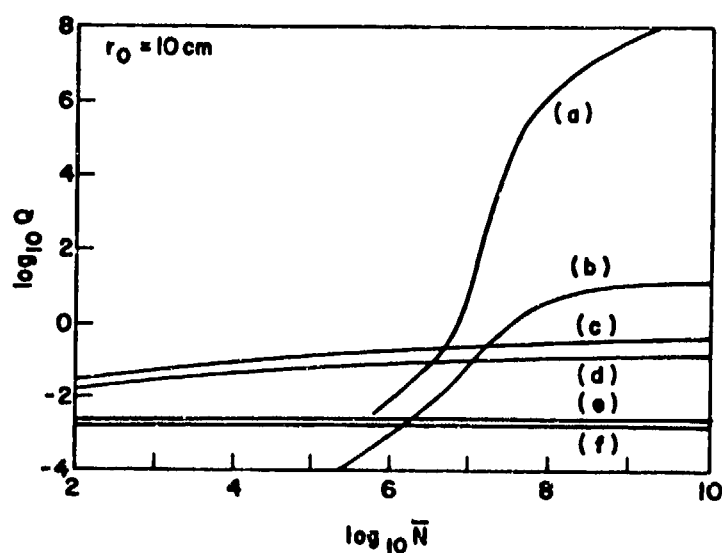


Fig. 5: Q vs. \bar{N} : (a) precompensation and postcompensation; (b) precompensation only; (c) tilt removal and postcompensation; (d) postcompensation only; (e) tilt removal only; (f) no compensation.

III. COMPARATIVE NOISE PERFORMANCE OF AMPLITUDE INTERFEROMETRY AND SPECKLE INTERFEROMETRY

In this section we present an analysis which compares the signal-to-noise performance of two techniques, one known as amplitude interferometry and the second known as speckle interferometry. In order to make this section as self contained as possible, we repeat certain portions of material presented in previous reports [1,2], but an attempt is made to keep this repetition to a minimum.

We assume that we desire to obtain information about a distant object, and that the atmosphere intervenes between our observation instrument (a telescope) and that object. Both techniques of interest are used to recover only partial information about the object - namely, we wish to estimate the strength of the squared modulus of the Fourier spectrum of the object. For the techniques of concern here, no attempt is made to recover the phase of the object spectrum.

A. SPECKLE INTERFEROMETRY

By the term "speckle interferometry", we mean the technique introduced by Labeyrie [3] which depends on averaging the "energy spectra" (squared moduli of the Fourier transforms) of a sequence of κ short-exposure photographs. By the term "amplitude interferometry", we mean the general class of techniques which, by the insertion of masks or wavefront folding prisms, operates the telescope as a Fizeau stellar interferometer or a set of Fizeau stellar interferometers with different aperture spacings. Examples are the interferometers of Currie [4] and of Breckinridge [5].

Considering first the case of speckle interferometry, the predictions of signal-to-noise ratio performance are based on a specific model of

the photodetection process which takes into account only the noise generated by the finite number of photons utilized in the recording of the image data and noise introduced by atmospheric fluctuations. The image $d_j(\vec{x})$ detected on the j^{th} exposure (exposure time assumed short compared with the fluctuation time of the atmosphere) is modeled as an inhomogeneous Poisson process. The form of the j^{th} detected image is thus

$$d_j(\vec{x}) = \sum_{k=1}^{N_j} \delta(\vec{x} - \vec{x}_{kj}) \quad (11)$$

where each δ -function represents a discrete photoevent, and \vec{x}_{kj} is the location on the spatial detector of the k^{th} photoevent. N_j represents the total number of photoevents recorded during the j^{th} exposure. This inhomogeneous Poisson process is taken to have a rate $\lambda_j(\vec{x})$ which is proportional to the classical image intensity $i_j(\vec{x})$ incident on the detector during the j^{th} exposure interval,

$$\lambda_j(\vec{x}) = \frac{\eta T}{h\nu} i_j(\vec{x}) \quad (12)$$

where

η is the quantum efficiency of the detector;

T is the image measurement time (assumed identical for all images);

h is Planck's constant; and

$\bar{\nu}$ is the mean optical frequency.

The speckle interferometry technique involves the following initial steps:

1. Each detected image $d_j(\vec{x})$ is Fourier transformed to produce a 2-D spectrum $D_j(\vec{\nu})$, where

$$D_j(\vec{v}) = \int_{-\infty}^{\infty} d_j(\vec{x}) e^{-i2\pi(\vec{x} \cdot \vec{v})} d\vec{x} \quad (13)$$

2. The squared modulus of each such spectrum is taken, producing $|D_j(\vec{v})|^2$;
3. These "energy spectra" are averaged over the set of κ independent pictures,

$$\langle |D(\vec{v})|^2 \rangle = \frac{1}{\kappa} \sum_{j=1}^{\kappa} |D_j(\vec{v})|^2 \quad (14)$$

Evaluation of the expected value of $\langle |D(\vec{v})|^2 \rangle$ shows [2] that it can be expressed as

$$E[\langle |D(\vec{v})|^2 \rangle] = \bar{N} + (\bar{N})^2 \hat{\phi}_i(\vec{v}) \quad (15)$$

where

\bar{N} is the expected number of photoevents in a single detected image, and

$\hat{\phi}_i(\vec{v})$ represents the expected value of the energy spectrum of the classical image intensity incident on the detector, normalized so that $\hat{\phi}_i(0) = 1$.

In turn, we can express $\hat{\phi}_i(\vec{v})$ as

$$\hat{\phi}_i(\vec{v}) = E[|\hat{B}_j(\vec{v})|^2] |\hat{O}(\vec{v})|^2 \quad (16)$$

where $\hat{B}_j(\vec{v})$ is the optical transfer function of the atmosphere-telescope combination on the j^{th} exposure, and $|\hat{O}(\vec{v})|^2$ is the energy spectrum of the true object radiance distribution $o(\vec{x})$, but normalized such that $|\hat{O}(0)|^2 = 1$.

If we assume that the telescope diameter D is much greater than

Fried's atmospheric coherence diameter r_0 ($D/r_0 \gg 1$), then in the mid-frequency region of the telescope OTF it is known [3] that

$$E[|\hat{B}_j(\vec{v})|^2] \cong \left(\frac{r_0}{D}\right)^2 \hat{B}_T(\vec{v}) \quad (17)$$

where $\hat{B}_T(\vec{v})$ represents the telescope OTF. Combining (15), (16) and (17), we find that a reasonable unbiased estimate of $|\hat{O}(\vec{v})|^2$ is given by

$$\widetilde{|\hat{O}(\vec{v})|^2} = \frac{\langle |D(\vec{v})|^2 \rangle - \bar{N}}{(\bar{N})^2 \left(\frac{r_0}{D}\right)^2 \hat{B}_T(\vec{v})} \quad (18)$$

In assessing the performance of the estimator of Eq.(18), we must find its variance for a given finite κ . If in the end we wish to express a signal-to-noise ratio associated with this estimator, we can equally well calculate the signal-to-noise ratio associated with $|D(\vec{v})|^2$. Fluctuations are expected in our estimate due to the finite number of photoevents detected and due to fluctuations of the atmosphere from picture to picture. The variance $\sigma_{|D|^2}^2$ associated with a single measured value of $|D|^2$ has been shown [1,2] to be

$$\begin{aligned} \sigma_{|D|^2}^2 = & \bar{N} + (\bar{N})^2 + 2(2+\bar{N})(\bar{N})^2 \hat{\phi}_i(\vec{v}) \\ & + (\bar{N})^2 \hat{\phi}_i(2\vec{v}) + (\bar{N})^2 \hat{\phi}_i^2(\vec{v}) \end{aligned} \quad (19)$$

Removing the bias from the expected value of $|D|^2$ in Eq.(15), the rms signal-to-noise ratio associated with a single frame becomes

$$\left(\frac{S}{N}\right)^{(1)} = \frac{E[|D|^2] - \bar{N}}{\sigma |D|^2} \quad (20)$$

$$= \frac{\bar{n} \hat{B}_T(\vec{v}) |\hat{O}(\vec{v})|^2}{\left\{ \left[1 + \bar{n} \hat{B}_T(\vec{v}) |\hat{O}(\vec{v})|^2 \right]^2 + \frac{1}{\bar{N}} \left[1 + 4\bar{n} \hat{B}_T(\vec{v}) |\hat{O}(\vec{v})|^2 + \bar{n} \hat{B}_T(2\vec{v}) |\hat{O}(2\vec{v})|^2 \right] \right\}^{1/2}}$$

where $\bar{n} = \left(\frac{r_0}{b}\right)^2 \bar{N}$ represents the average number of photoevents per frame per atmospheric coherence area. If the κ detected frames are recorded with independent realizations of the atmospheric transfer function, the rms signal-to-noise ratio associated with κ frames becomes

$$\left(\frac{S}{N}\right)^{(\kappa)} = \sqrt{\kappa} \left(\frac{S}{N}\right)^{(1)} \quad (21)$$

These results are consistent with those obtained earlier by Roddier [6].

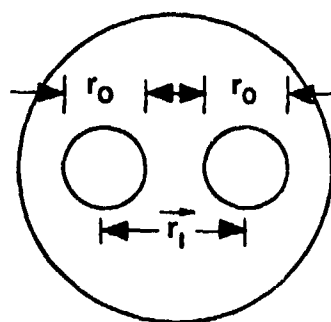
B. AMPLITUDE INTERFEROMETER

For the case of amplitude interferometry, several different measurement configurations can be imagined. Two such configurations are considered here, and the signal-to-noise ratios achieved are shown to be equal. Nonetheless, this signal-to-noise ratio is different than that achieved by speckle interferometry.

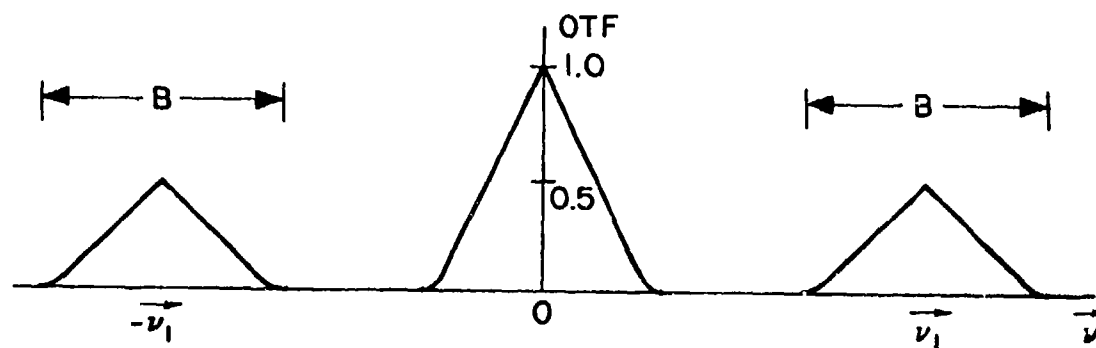
The first method of interest is obtained with only a slight modification of the speckle interferometry technique. We insert a mask in the aperture of the telescope; the mask contains two circular openings, each of diameter approximately r_0 [7] and separated by a fixed vector distance \vec{r}_1 , as shown in Fig. 6(a). The corresponding diffraction-limited telescope OTF has the form shown in Fig. 6(b). The center frequency \vec{v}_1 of the two bandpass islands of the OTF is given by

$$\pm \vec{v}_1 = \pm \frac{\vec{r}_1}{\bar{\lambda} F} \quad (22)$$

where F is the telescope focal length and $\bar{\lambda}$ the mean wavelength.



(a)



(b)

Fig. 6: Amplitude interferometer

- (a) pupil plane mask:
- (b) OTF

The bandwidth of these islands is

$$B = \frac{2r_0}{\lambda F}, \quad (23)$$

and the peak amplitude is $1/2$.

A sequence of κ pictures is taken, each with an exposure time short compared to the fluctuation time of the atmosphere. The resulting photon-limited images are Fourier transformed, and the squared moduli of these transforms are averaged over the set of pictures, as before. The effect of the atmosphere on any given picture is more simple in this case than in the previous case of more general speckle imaging. If the scintillation effects introduced by propagation through the atmosphere are negligibly small, then, due to the fact that the individual aperture openings are of size r_0 , the only effect of the atmosphere is to randomly shift the phase of all Fourier components within the bandpass spectrum by a fixed amount. This phase shift is identical for all frequency components within the spectral island, but it changes from frame to frame.

The signal-to-noise ratio associated with the estimate $\widetilde{|\hat{O}(\vec{v}_1)|^2}$ differs from that achieved in the previously considered speckle imaging case. One reason for the difference is the different effect that the atmosphere has on the detected images, as mentioned above. A second reason arises from the fact that the collecting area of the speckle imaging system is $\pi D^2/4$ while the collecting area in the present case is only $\pi r_0^2/2$.

If we remove terms introduced by the fluctuating amplitude of the atmospherically-induced OTF, the variance of $|D|^2$ becomes

$$\sigma_{|D|^2}^2 = 2\bar{n} + 4(\bar{n})^2 + 16(\bar{n})^2\hat{\phi}_i + 16(\bar{n})^3\hat{\phi}_i \quad (24)$$

where we have taken account of the fact that the average number of photoevents detected per frame is now $2\bar{n}$. The expected value of $|D|^2$ is in this case given by

$$E[|D|^2] = 2\bar{n} + 4(\bar{n})^2\hat{\phi}_i \quad (25)$$

Removing the bias from this expected value, and noting that

$$\hat{\phi}_i(\vec{r}_1) = |B_T(\vec{r}_1)|^2 |\hat{O}(\vec{r}_1)|^2 = \frac{1}{4} |\hat{O}(\vec{r}_1)|^2, \quad (26)$$

we obtain for the single-frame rms signal-to-noise ratio

$$\frac{S}{N}^{(1)} = \frac{\bar{n} |\hat{O}(\vec{r}_1)|^2 / 2}{\left\{ 1 + \frac{1}{2\bar{n}} + (1+\bar{n}) |\hat{O}(\vec{r}_1)|^2 \right\}^{1/2}} \quad (27)$$

A disadvantage of the above measurement technique is that only one spacing \vec{r}_1 can be explored at one time. More desirable would be a system that allows many different fringes to be detected at one time. Such a system has been proposed by Currie. The wavefront from the full unobstructed telescope aperture passes through a wavefront folding interferometer, as illustrated in Figure 7. A detector placed at a single point at the output of the wavefront folding interferometer detects the



Fig. 7: Amplitude interferometer

interference of light from two points on the telescope aperture, those points being located at 180° relative angular rotation about the center of the telescope mirror. An entire array of detectors at the output of the wavefront folding interferometer thus detects simultaneously the interference between many different pairs of points, each pair being separated by a different vector spacing \vec{r} . If a frequency shifter is placed in one arm of the wavefront folding interferometer, each detector will see an oscillating intensity, the amplitude of which is a direct measure of the amplitude of the object spectrum at the corresponding spatial frequency.

The output $d(t)$ of a given detector is subjected to an electronic measurement system as shown in Fig. 8. The frequency ω_0 corresponds to the angular frequency shift introduced in one arm of the interferometer. The system shown detects the in-phase and quadrature components of the oscillating signal, and combines these to estimate the squared magnitude of the fringe amplitude. It is again assumed that a single detector sees light collected from two wavefront patches, each of diameter r_0 .

The measured quantity $Z = C^2 + S^2$ can be shown to have the following mean and variance:

$$\begin{aligned}\bar{Z} &= 2\bar{n} + (\bar{n})^2 |\hat{O}(\vec{v})|^2 \\ \sigma_Z^2 &= 2\bar{n} + 4(\bar{n})^2 + 4(\bar{n})^2 |\hat{O}(\vec{v})|^2 + 4(\bar{n})^3 |\hat{O}(\vec{v})|^2\end{aligned}\tag{28}$$

Removing the bias from Z , we obtain an rms signal-to-noise ratio (based on a single integration interval that is short compared to the fluctuation time of the atmosphere)

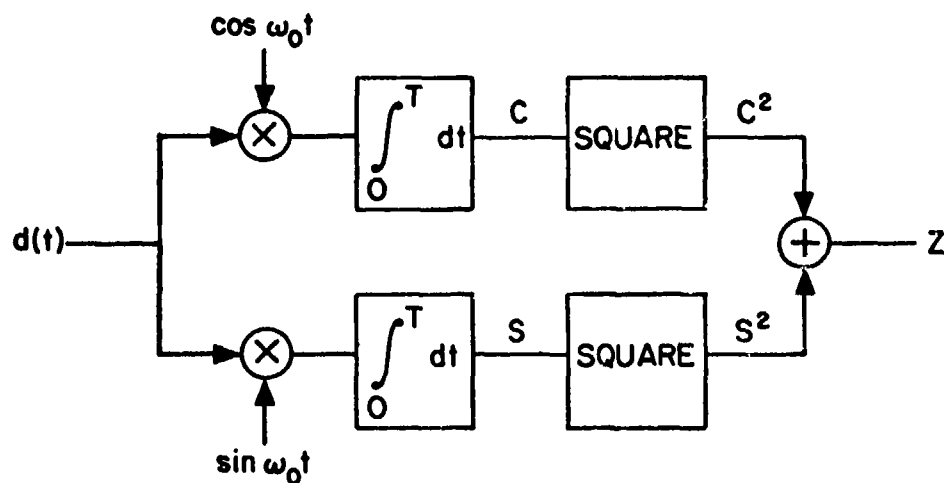


Fig. 8: Fringe contrast detector

$$\frac{S}{N}^{(1)} = \frac{\bar{Z} - 2\bar{n}}{\sigma_Z} = \frac{\bar{n} |\hat{O}(\vec{v})|^2 / 2}{\left\{ 1 + \frac{1}{2\bar{n}} + (1 + \bar{n}) |\hat{O}(\vec{v})|^2 \right\}^{1/2}} \quad (29)$$

which is identical with the result obtained previously.

C. COMPARISON OF SPECKLE AND AMPLITUDE INTERFEROMETRY

We now compare the single-frame rms signal-to-noise ratios appropriate for speckle and amplitude interferometry. In making the comparison, we assume that the optical bandwidths, integration times and optical efficiencies of the two systems are identical. In addition, we assume [8] that the detectors for the two systems have identical quantum efficiencies.

Figure 9 shows plots of the single-frame rms signal-to-noise ratio for a point-source object ($|\hat{O}(\vec{v})|^2 = 1$). For the case of the speckle interferometer we assume that $v/v_0 = 0.8$ ($v_0 =$ diffraction-limited

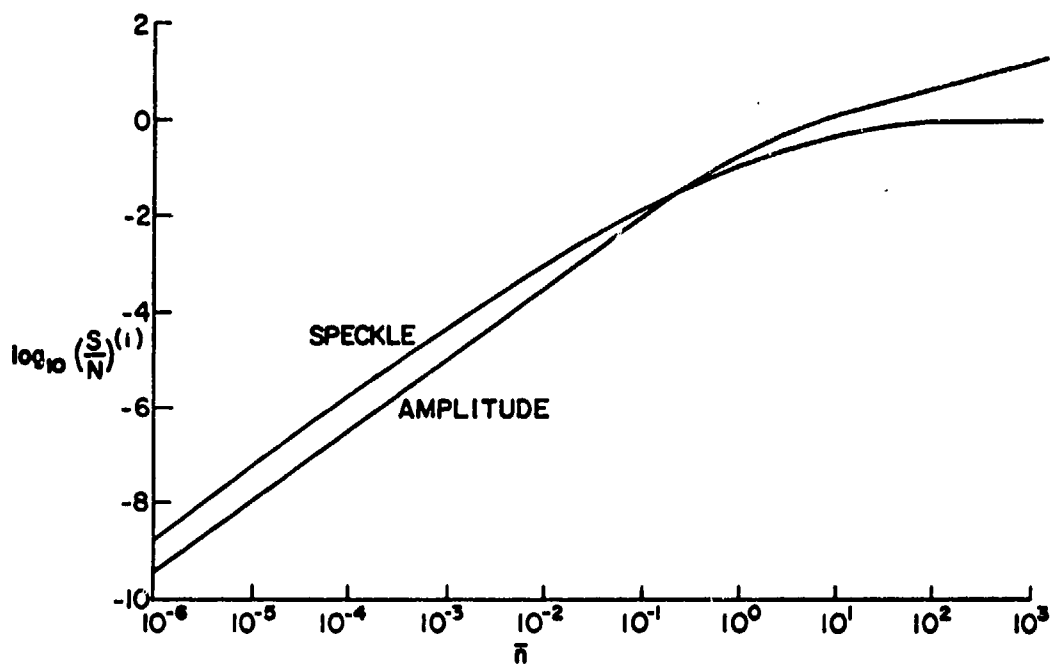


Fig. 9: Signal-to-noise ratios, speckle
vs. amplitude interferometer,
 $|\hat{0}|^2 = 1$

cutoff frequency) and $D/r_0 = 16$ (1.6 meter telescope diameter with $r_0 = 10$ cm). The chief conclusions to be drawn from these curves are:

1. For $\bar{n} \ll 1$, the rms signal-to-noise ratios of both techniques increase in proportion to $(\bar{n})^{3/2}$.

$$\text{amplitude } \frac{S}{N}^{(1)} \cong \frac{(\bar{n})^{3/2}}{2\sqrt{2}}$$

$$\text{speckle} - \frac{S}{N}^{(1)} \cong (\bar{n})^{3/2} \cdot \frac{D}{r_0} \hat{B}_T$$

For the parameters chosen here speckle interferometry is superior to amplitude interferometry in this range by a factor of 4.7;

2. For \bar{n} in the range $0.1 < \bar{n} < 1.0$, the curves cross, and amplitude interferometry becomes superior to speckle interferometry;
3. For $\bar{n} \gg 1$, the $\frac{S}{N}^{(1)}$ for speckle interferometry asymptotically approaches unity, never exceeding that value, while for amplitude interferometry it continues to increase as $\sqrt{\bar{n}}/2$ indefinitely.

In Figure 10 we show the corresponding curves for $v/v_0 = 0.8$, $D/r_0 = 16$, but a much smaller object spectrum $|\hat{O}|^2 = 10^{-4}$. For very small values of \bar{n} , speckle interferometry remains superior to amplitude interferometry, but by a smaller margin than previously. In the vicinity of $\bar{n} = 10^{-2}$ for speckle interferometry and $\bar{n} = 1$ for amplitude inter-

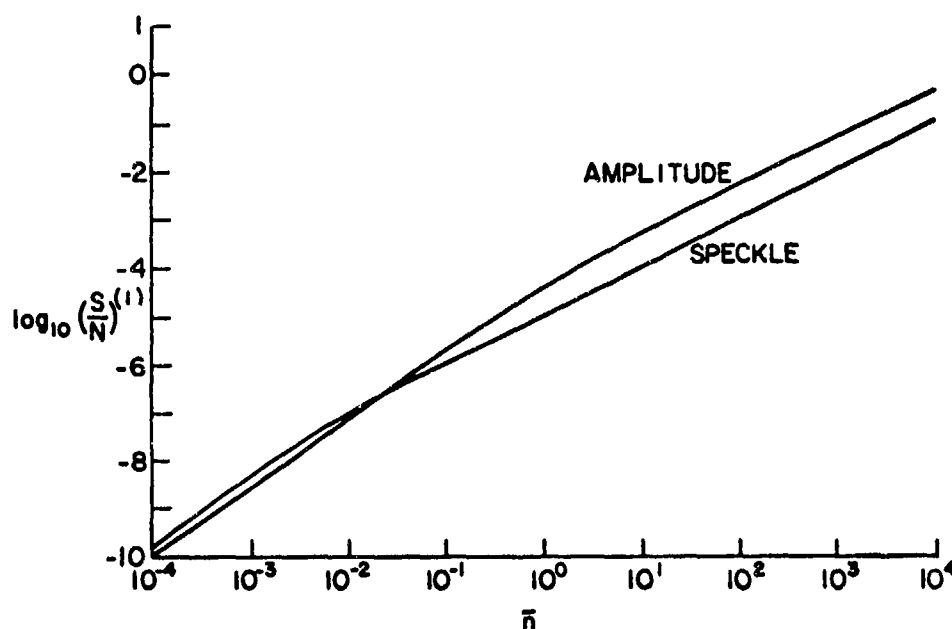


Fig. 10: Signal-to-noise ratio, speckle vs. amplitude interferometry
 $|\hat{O}|^2 = 10^{-4}$.

ferometry, both curves change from an $(\bar{n})^{3/2}$ increase to an \bar{n} increase, with amplitude interferometry superior to speckle interferometry. Eventually, for values of \bar{n} so large as to be off this figure, the speckle interferometry curve will saturate at value unity, while the amplitude interferometry curve will begin to increase in proportion to $\sqrt{\bar{n}}$.

IV. SPACE-VARIANT AND NONLINEAR RESTORATION TECHNIQUES

Our past work on the restoration of photon-limited, blurred images has considered only the case of linear, space-invariant restoration filters. Based on the intuitive feeling that improved restorations can be obtained with linear space-variant filters and nonlinear filters, we have begun to explore such possibilities. The question which is of major concern here is how much improvement in restoration filter performance can be achieved by going to the decidedly more complex space-variant and nonlinear restoration schemes. Our work in this area has progressed at least to the point where the formulation of the problem has become clearer.

In anticipation that future technical reports will detail this work more thoroughly, we mention here the current state of our knowledge, without any specific "proofs" of the results stated.

The most general formulation of the linear least-squares filtering problem can be appreciated by reference to Figure 11. For simplicity, we treat space as a one-dimensional variable x , the results being easily generalized to two dimensions. The object radiance distribution $o(x)$ is assumed to be a random process, but for generality it is allowed to have space-variant or non-stationary statistics. The object $o(x)$

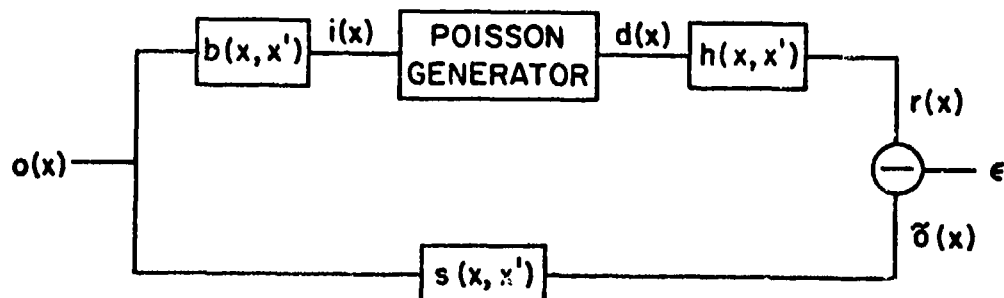


Fig. 11: Space-variant least-squares filtering

is degraded by a linear blur with space-variant point spread function $b(x, x')$. This blurred image is then converted to a detected image by passage through the "Poisson generator", which generates an inhomogeneous Poisson impulse process, with rate $\lambda(x)$ proportional to the classical image intensity,

$$\lambda(x) = \frac{nT}{h\nu} i(x) \quad (30)$$

The detected image then passes through a linear, possibly space-variant, restoration filter with impulse response $h(x, x')$. The impulse response $h(x, x')$ is chosen to minimize the mean square error between the restored image $r(x)$ and an "ideally filtered" version of the object, $\tilde{o}(x)$. The ideal filter may in general be space-variant, and its impulse response is represented by $s(x, x')$.

Without presenting a proof, we simply state that the impulse response of the optimum restoration filter can be shown to be a function $h(x, x'')$ satisfying the integral equation

$$\begin{aligned} \int_{-\infty}^{\infty} h(x, x'') R_d(x', x'') dx'' \\ = \int_{-\infty}^{\infty} s(x, x'') R_{do}(x', x'') dx'' \end{aligned} \quad (31)$$

where

$$\begin{aligned} R_d(x', x'') &= E[d(x')d(x'')] \\ R_{do}(x', x'') &= E[d(x')o(x'')] \end{aligned} \quad (32)$$

In turn, the correlation functions of interest can be expressed as

$$\begin{aligned} R_d(x', x'') &= \frac{\eta T}{h\nu} \bar{i}(x) \delta(x' - x'') + \frac{\eta T^2}{h^2 \nu^2} R_i(x', x'') \\ R_{do}(x', x'') &= \frac{\eta T}{h\nu} R_{io}(x', x'') \end{aligned} \quad (33)$$

where

$$\begin{aligned} R_i(x', x'') &= E[i(x')i(x'')] \\ R_{io}(x', x'') &= E[i(x')o(x'')] \end{aligned} \quad (34)$$

Finally we note that

$$i(x) = \int_{-\infty}^{\infty} b(x, x'') o(x'') dx'' \quad (35)$$

A case of major interest is obtained if the blur spread function b and the ideal spread function s are space-invariant, but the object itself is non-stationary. Since the objects of prime interest here are of finite size, they must of necessity have spatially non-stationary

statistics. The correlation functions of interest become

$$R_i(x', x'') = \iint_{-\infty}^{\infty} b(x' - \xi) b(x'' - \eta) R_0(\xi, \eta) d\xi d\eta \quad (36)$$

$$R_{i0}(x', x'') = \int_{-\infty}^{\infty} b(x' - \xi) R_0(\xi, x'') d\xi$$

where $R_0(\xi, x'')$ is the autocorrelation function of the non-stationary object.

In some cases it is possible to argue that the object is non-stationary primarily by virtue of a non-stationary second moment. In such cases, the autocorrelation function of the object takes the approximate form

$$R_0(x', x'') \cong \Gamma_0\left(\frac{x' + x''}{2}\right) \gamma_0(x' - x'') \quad (37)$$

The idealized case of an object with a "white" spectrum yields the autocorrelation function

$$R_0(x', x'') \cong \Gamma_0\left(\frac{x' + x''}{2}\right) \delta(x' - x'') \quad (38)$$

An additional case of interest is that of a stationary object multiplied by a "window" function $w(x)$. If $r_0(x' - x'')$ represents the autocorrelation function of the original stationary object, the autocorrelation of the windowed object is

$$R_0(x', x'') = w(x') w(x'') r_0(x' - x'') \quad (39)$$

It is perhaps worth special mention here that, if the blur filter and the ideal filter are space-invariant and the object is statistically stationary, then we can show from the results presented above that the filter which achieves minimum mean-square error is always the space-invariant filter derived in our previous reports [1,2]. Such a filter

remains optimum in spite of the signal-dependent character of Poisson noise.

In addition to the linear space-variant filters discussed above, we are also beginning preliminary studies of the nonlinear filter shown in Fig. 12(a). In this case the filter is taken to be linear and space-invariant, with the transfer function (see Eq.(4))

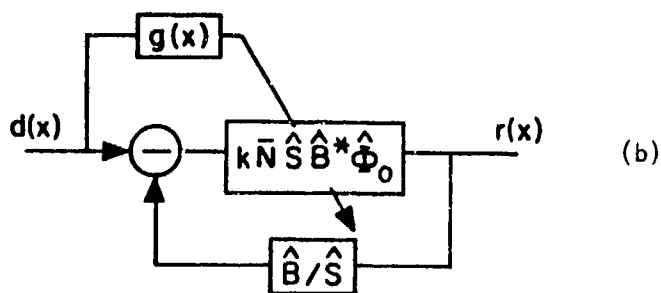
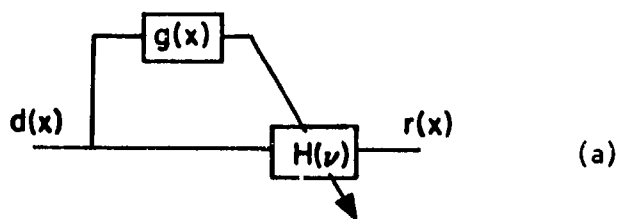


Fig. 12: Realization of non-linear filter
(a) direct; (b) with feedback

$$\hat{H}(v) = \frac{k\bar{N} \hat{S} \hat{B} * \hat{\phi}_0}{1 + \bar{N} |\hat{B}|^2 \hat{\phi}_0}$$

appropriate for minimizing mean-squared error. However, the parameter \bar{N} is no longer taken to be equal to the average number of photoevents in the entire image. Rather, the detected image $d(x)$ is passed through a linear, invariant smoothing filter with impulse response $g(x)$, the purpose of which is to produce a local average value of \bar{N} . Thus \bar{N} is a function of x , and the filter parameter is chosen appropriately for the local photon environment. In regions of the picture where there have been very few photoevents, very little enhancement will be attempted, but in regions where the number of photoevents is large, greater enhancement is attempted. Such a filter has a characteristic that is highly dependent on the detected signal $d(x)$; it is this signal-dependent character that causes the filter to be nonlinear. There is no doubt that such a filter can perform better than any linear filter in restoring photon-limited images. The key questions are how much better it can perform, and whether the increased performance is worth the extra computational complexity involved. As a potentially helpful fact, we note that the required transfer function can be realized by the feedback structure of Fig. 12(b), where the parameter \bar{N} is controlled simply by varying the gain of the feed-forward filter.

Work on the topics outlined in this section is still in progress and will be reported on in greater detail in our next technical report.

REFERENCES

1. J.W. Goodman and J.F. Belsher, "Photon Limited Images and their Restoration", RADC-TR-76-50, March 1976, (A024027).
2. J.W. Goodman and J.F. Belsher, "Precompensation and Postcompensation of Photon Limited Degraded Images", RADC-TR-76-382, December 1976.
3. A. Labeyrie, Astron. and Astrophys. 6, 85 (1970).
4. D.G. Currie, private communication.
5. J.B. Breckinridge, "Obtaining Information through the Atmosphere at the Diffraction Limit of a large Aperture", J.O.S.A., 65, 755-759, July 1975.
6. F. Roddier, "Signal-to-Noise Ratio in Speckle Interferometry Imaging in Astronomy", (Technical Digest), Topical Meeting of the Optical Society of America on Imaging in Astronomy, June 1975.
7. We assume that the diameters can be made as large as r_0 . However, eliminating the effects of wavefront tilt over the individual apertures may require somewhat smaller openings.
8. If any of these assumptions should prove to be false, the curves for speckle and amplitude interferometry must be moved horizontally with respect to each other.

METRIC SYSTEM

BASE UNITS:

Quantity	Unit	SI Symbol	Formula
length	metre	m	...
mass	kilogram	kg	...
time	second	s	...
electric current	ampere	A	...
thermodynamic temperature	kelvin	K	...
amount of substance	mole	mol	...
luminous intensity	candela	cd	...

SUPPLEMENTARY UNITS:

plane angle	radian	rad	...
solid angle	steradian	sr	...

DERIVED UNITS:

Acceleration	metre per second squared	...	m/s
activity (of a radioactive source)	disintegration per second	...	(disintegration)/s
angular acceleration	radian per second squared	...	rad/s
angular velocity	radian per second	...	rad/s
area	square metre	...	m
density	kilogram per cubic metre	...	kg/m
electric capacitance	farad	F	A·s/V
electrical conductance	siemens	S	A/V
electric field strength	volt per metre	...	V/m
electric inductance	henry	H	V·s/A
electric potential difference	volt	V	W/A
electric resistance	ohm	...	V/A
electromotive force	volt	V	W/A
energy	joule	J	N·m
entropy	joule per kelvin	...	J/K
force	newton	N	kg·m/s
frequency	hertz	Hz	(cycle)/s
illuminance	lux	lx	lm/m
luminance	candela per square metre	...	cd/m
luminous flux	lumen	lm	cd·sr
magnetic field strength	ampere per metre	...	A/m
magnetic flux	weber	Wb	V·s
magnetic flux density	tesla	T	Wb/m
magnetomotive force	ampere	A	...
power	watt	W	J/s
pressure	pascal	Pa	N/m
quantity of electricity	coulomb	C	A·s
quantity of heat	joule	J	N·m
radiant intensity	watt per steradian	...	W/sr
specific heat	joule per kilogram-kelvin	...	J/kg·K
stress	pascal	Pa	N/m
thermal conductivity	watt per metre-kelvin	...	W/m·K
velocity	metre per second	...	m/s
viscosity, dynamic	pascal-second	...	Pa·s
viscosity, kinematic	square metre per second	...	m/s
voltage	volt	V	W/A
volume	cubic metre	...	m
wavenumber	reciprocal metre	...	(wave)/m
work	joule	J	N·m

SI PREFIXES:

Multiplication Factors	Prefix	SI Symbol
1 000 000 000 000 = 10 ¹²	tera	T
1 000 000 000 = 10 ⁹	giga	G
1 000 000 = 10 ⁶	mega	M
1 000 = 10 ³	kilo	k
100 = 10 ²	hecto*	h
10 = 10 ¹	deka*	da
0.1 = 10 ⁻¹	deci*	d
0.01 = 10 ⁻²	centi*	c
0.001 = 10 ⁻³	milli	m
0.000 001 = 10 ⁻⁶	micro	μ
0.000 000 001 = 10 ⁻⁹	nano	n
0.000 000 000 001 = 10 ⁻¹²	pico	p
0.000 000 000 000 001 = 10 ⁻¹⁵	femto	f
0.000 000 000 000 000 001 = 10 ⁻¹⁸	atto	a

* To be avoided where possible.

*MISSION
of
Rome Air Development Center*

RADC plans and conducts research, exploratory and advanced development programs in command, control, and communications (C³) activities, and in the C³ areas of information sciences and intelligence. The principal technical mission areas are communications, electromagnetic guidance and control, surveillance of ground and aerospace objects, intelligence data collection and handling, information system technology, ionospheric propagation, solid state sciences, microwave physics and electronic reliability, maintainability and compatibility.

